HHS Public Access

Author manuscript

J Biophotonics. Author manuscript; available in PMC 2018 October 13.

Published in final edited form as:

J Biophotonics. 2018 April ; 11(4): e201700204. doi:10.1002/jbio.201700204.

Multicontrast endomyocardial imaging by single-channel high-resolution cross-polarization optical coherence tomography

Xinwen Yao[1], **Yu Gan**[1], **Yuye Ling**[1], **Charles C. Marboe**[2], and **Christine P. Hendon**[1,*]

[1]Department of Electrical Engineering, Columbia University, New York, New York

[2]Department of Pathology and Cell Biology, Columbia University Medical Center, New York, New York

Abstract

A single-channel high-resolution cross-polarization (CP) optical coherence tomography (OCT) system is presented for multicontrast imaging of human myocardium in one-shot measurement. The intensity and functional contrasts, including the ratio between the cross- and co-polarization channels as well as the cumulative retardation, are reconstructed from the CP-OCT readout. By comparing the CP-OCT results with histological analysis, it is shown that the system can successfully delineate microstructures in the myocardium and differentiate the fibrotic myocardium from normal or ablated myocardium based on the functional contrasts provided by the CP-OCT system. The feasibility of using A-line profiles from the 2 orthogonal polarization channels to identify fibrotic myocardium, normal myocardium and ablated lesion is also discussed.

Graphical Abstract

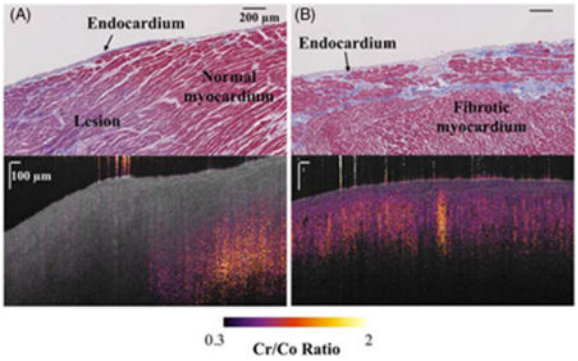

Keywords

imaging systems; medical and biological imaging; myocardium imaging; optical coherence tomography; polarization-selective devices; tissue characterization

[*]**Correspondence:** Christine P. Hendon, Department of Electrical Engineering, Columbia University, 500 West 120th Street, Mudd 1310, New York, NY 10027. cpf2115@columbia.edu.

1 | INTRODUCTION

Garnering the knowledge of myocardial structure and tissue composition is crucial for understanding the cardiac mechanical and electrical function. In clinical settings, the myocardium is assessed by various techniques, including histological analysis of endomyocardial biopsy (EMB) or autopsy samples, and noninvasive imaging modalities such as cardiac magnetic resonance, echocardiography and computed tomography [1–3]. EMB is currently the gold standard for transplant rejection monitoring, as well as prognosis and treatment of some specific myocardial disorders like unexplained ventricular arrhythmias and heart failure [4]. During EMB, multiple biopsy samples, typically 1 to 2 mm in depth, are taken from the right ventricular septum (RVS) on a routine basis [4]. However, this destructive procedure has been shown to be associated with clinical complications, potential long-term sequelae, and importantly, can suffer from sampling artifacts in the case of focal disease [4–6]. On the contrary, most noninvasive imaging modalities have low resolution, and some may require a long imaging duration. Therefore, there is a need to develop new tools to assess myocardial substrates with HR.

As a high-resolution (HR), high-speed and nondestructive imaging modality, optical coherence tomography (OCT) has been demonstrated in myocardial imaging in both ex vivo [7–16] and in vivo settings [17–19], and holds promise to be translated to the clinics [20]. It has been reported that myofiber orientation within the myocardium, which has been seen in Magnetic resonance imaging (MRI) images [21, 22], can be well identified by using OCT intrinsic intensity contrast [7–9, 12], too. By increasing the resolutions of OCT system, more features in myocardium like Purkinje fibers may be unveiled in the intensity contrast [10]. However, it is difficult to differentiate fibrotic myocardium against normal myocardium solely from the OCT intrinsic contrast. Recently, we have developed an automated classification algorithm for human endomyocardial OCT images, in which thickened endocardium and adipose tissue could be well identified through automated method [23]. Yet, the classification accuracy of fibrotic myocardium is less than satisfactory, due to the subtle difference in OCT intensity and texture contrasts between normal myocardium and fibrotic myocardium. Therefore, additional features that can depict tissue composition are still desired to further improve the classification performance for fibrotic myocardium.

Polarization contrast could very well serve this purpose, since it is known that normal myocardium manifests tissue birefringence. By using polarization sensitive techniques, it is possible to provide additional polarization-based contrast for the structure and tissue composition of myocardium [13, 14, 24, 25]. Changes in the myocardial tissue composition may disrupt the normal organization of myofiber bundles, which are reflected through the polarization contrast. This change of the polarization contrast can be used for characterization of myocardial infarction [16], and lesions created by radio-frequency ablation (RFA) [17, 20, 24]. A few second harmonic generation imaging studies on fibrotic myocardium have indicated that increased amount of entangled and less orderly collagen fibers deposition were found within the myofibers, resulting in the interruption of the birefringence of the normal myocardium [26, 27]. Disruption of birefringence artifact within the intrinsic intensity OCT images was also observed when imaging fibrotic myocardium by using a regular HR spectral domain-OCT system without polarization selective detection

[10]. These findings suggest that myocardial fibrosis may be differentiated in OCT with the addition of polarization-based contrast.

As one of the polarization sensitive techniques, crosspolarization (CP) OCT system provides an alternative to access the tissue polarization properties in a simplified fashion. CP-OCT system uses linearly polarized light to interrogate the sample, usually nonbirefringent, and the loss of polarized backscattering is analyzed by comparing the signal strength from CP and co-polarization channels [28–32]. The loss of polarization, or depolarization effect, can be thus used as a contrast to localize the origin of depolarizers presented in tissue. It is worth noting that for the original CP-OCT system proposed by Schmitt and Xiang [28], the measurements were taken by a single detector in a time-multiplexed manner, where the reference arm was sequentially switched between the co- and cross-polarization states with respective to that of the sample arm. CP-OCT systems using similar schemes have been applied in oral tissue characterization [29], bladder cancer screening [30], atherosclerotic plaque assessment [31] and biofilm characterization [32]. These systems demonstrated the feasibility of qualitatively characterizing depolarization effect. However, the imaging speed was limited due to the switching, and the tissue birefringence property was not directly addressed in these CP-OCT systems.

In this work, we present a HR CP-OCT system that can provide functional contrast of human myocardial tissue in one-shot measurement. The system is implemented based on our previously reported HR-OCT system with minimal modifications. It features a broadband supercontinuum source, single-channel and one-shot detection. The system has an axial resolution of 3.07 μm, and lateral resolution of 5.52 μm. The intensity contrast together with the functional contrasts, including channel intensity ratio and cumulative retardation, can be reconstructed by using the complex Aline information from the cross- and co-polarization channels. Myocardium tissue specimens from fresh human hearts are imaged to demonstrate the CP-OCT contrasts. We show that tissue polarization properties, including the retardation and depolarization, can be quantitatively and qualitatively assessed by the CP-OCT system, respectively. By utilizing the functional contrasts of fresh human myocardial tissues, fibrotic myocardium can be successfully differentiated from normal myocardium and acute-ablated lesions. We also suggest the possibility of using A-line features from the 2 orthogonal polarization channels to distinguish normal myocardium, fibrotic myocardium and ablated lesions. This may serve as a rapid and cost-efficient solution for assessment of myocardium and further facilitate automatic tissue classification.

2 | METHOD

2.1 | HR CP-OCT system

Figure 1 shows the schematic of the HR CP-OCT system. It is constructed based on the Ultra-high resolution (UHR) system developed in our lab [10], which features a super-continuum source (SuperK EXTREME, NKT Photonics, Birkerød, Denmark), and has an axial resolution of 2.72 μm, a lateral resolution of 5.52 μm and a large imaging range of 1.78 mm. The supercontinuum is spectrally filtered to produce a broadband input spectrum with bandwidth larger than 150 nm. The focusing lens in the spectrometer is customized to accommodate a wavelength range of 200 nm with optimized focusing performance, and a

2048-pixel Charge-coupled device (CCD) line scan sensor is employed as the spectrometer detector, which features a maximum line rate of 70 kHz. The sensitivity of the system is 93 dB at 70 kHz. To transform it into a CP setup, the input supercontinuum source is vertically polarized by a thin-film linear polarizer (Thorlabs LPNIR050, Thorlabs, Newton, NJ, USA). The reference arm is split into 2 orthogonal polarization channels using a nonpolarized beam cube (Thorlabs BS011, Thorlabs, Newton, NJ, USA). An achromatic quarter wave plate (Thorlabs AQWP05M-980, Thorlabs, Newton, NJ, USA) is inserted into one of the reference arm, with its fast axis aligned at 45° with respect to the input polarization. The 2 reference mirrors RM1 and RM2 are offset by 0.87 mm in free space (equivalent to around 500 pixels) to optimize the imaging range of a single channel while maintaining a good image quality. The newly inserted optics are chosen to support broadband light as to maintain the original bandwidth of the light source.

Assuming the incident beam is linearly polarized at **y** direction as $\mathbf{E} = [0.1]^{T}$, the interferometric signal detected by the spectrometer after linear-k interpolation can be written as Eq. (1) [33]:

$$I_{\mathrm{OCT}}(k) = \sum_{n} S_x(z_n)\cos[2k(z_n - z_{\mathrm{rx}}) + \varphi_x(z_n)] + \sum_{n} S_y(z_n)\cos[2k(z_n - z_{\mathrm{rx}} + d) + \varphi_y(z_n)], \quad (1)$$

where, $S_x(z_n)$, $S_y(z_n)$ are the cross-correlation strengths of the backscattering signals from the sample depth z_n and the respective reference arms, $\varphi_x(z_n)$, $\varphi_y(z_n)$ are the phase terms of the signals from the respective polarization channels, z_{rx} is the single optical path length of the CP reference arm, and d is the single path length difference between the cross- and co-polarization reference arm. Both Direct current (DC) terms and the autocorrelation from the sample arm are ignored. After Fourier transform of $I_{\mathrm{OCT}}(k)$, the depth dependent magnitude $A_x(z)$, $A_y(z)$, and phase $\Phi_x(z)$, $\Phi_y(z)$ of the 2 orthogonal channels can be extracted from the processed complex A-line signals $I_{\mathrm{cr}}(z)$ and $I_{\mathrm{co}}(z)$ as

$$\begin{aligned} I_{\mathrm{cr}}(z) &= A_x(z - z_{\mathrm{rx}})\exp[i\,\Phi_x(z - z_{\mathrm{rx}})] \\ I_{\mathrm{co}}(z) &= A_y(z - z_{\mathrm{rx}} + d)\exp[i\,\Phi_y(z - z_{\mathrm{rx}} + d)] \end{aligned} \quad (2)$$

The A-line signals in Eq. (2) can be well separated in the spatial domain if the offset d between the 2 reference mirrors is large enough. Practically, because of the limited penetration depth in the myocardium for 800 nm light, the offset is set to be 0.87 mm (500 pixels), which is sufficient to avoid overlay of channel information while maintaining a good image quality.

It should be also noted that it is difficult to fully polarize the originally unpolarized broadband supercontinuum output by a thin-film linear polarizer. This leads to the cross-talk between the orthogonal polarization channels. The crosstalk is represented by a delta-

function at the location d in the spatial domain after inverse Fourier transform of $I_{OCT}(k)$ without dispersion compensation. Therefore, it can be easily filtered out in advance.

The complex A-line information of the 2 polarization channels can be individually extracted in the spatial domain by using a rectangular window with N pixels: the CP channel occupies the first N pixels, and the co-polarization channel occupies from $(d+1)$th to $(d+N)$ th pixels. Because of the finite pixel size, the actual offset d falls between the Mth and $(M+1)$th pixels, and a subpixel adjustment is necessary to well align the 2 polarization channels. This can be done by adding a calibration step, which will be discussed in detail in the next session.

To further understand the magnitude and phase information of the 2 orthogonal polarization channels in Eq. (2), the signals detected by the cross- and co-polarization channels can be reconstructed following the method adopted in polarization-sensitive (PS) OCT techniques. For the 800 nm wavelength region, where the signal penetration depth is usually limited to a few hundreds of microns into the tissue, the biological samples that manifest birefringence can be modeled as an arbitrary wave retarder with uniform optic axis along the depth. The tissue birefringence can be modeled by the Jones matrix of a general retarder of retardation δ and optic axis orientation θ as [34]

$$\mathbf{J}(\delta,\theta) = \begin{bmatrix} \cos^2\theta + \sin^2\theta\exp(-i\delta) & \cos\theta\sin\theta(1-\exp(-i\delta)) \\ \cos\theta\sin\theta(1-\exp(-i\delta)) & \sin^2\theta + \cos^2\theta\exp(-i\delta) \end{bmatrix}, \quad (3)$$

where, δ and θ represent the cumulative retardation and optic axis orientation from the sample surface to the imaging depth, respectively. In CP-OCT configuration, the linearly polarized light directly interrogates the sample. The Jones vector of the backscattered sample beam $\overrightarrow{\mathbf{E}_{sn}}$ from depth z_n at the exit of the interferometer can be written as Eq. (4), where $R(z_n)$ represents the reflectivity at the sample depth z_n. As shown in Eq. (4), the cumulative retardation δ and optic axis orientation θ of the birefringent tissue mutually affect the complex signals of the cross- and co-polarization channels. Therefore, rotational adjustment of the polarization state alignment with respect to the tissue can be carried out to optimize the CP channel contrast for imaging birefringent tissues.

2.2 | Signal processing

The flow chart of signal processing steps is presented in Figure 2A. Generally, the CP-OCT signals are extracted by following the OCT signal processing steps as described in Ref. [10], including background subtraction, linear-k interpolation, spectral shaping and numerical dispersion compensation. Because of the existence of the cross-talk between the orthogonal polarization channels (RM1 and RM2) due to the imperfection of the linear polarizer, the autocorrelation of the reference arm is filtered out from the raw spectra prior to the dispersion compensation process.

The linear-in-k, dispersion-free spectra $I'_{k}(n)$ are duplicated into 2 copies: one as the CP channel $II'_{k\_cr}(n)$ and the other as the co-polarization channel $I'_{k\_co}(n)$. After inverse Fourier

transform, a window size of 450 pixels (equivalent to around 0.78 mm in depth) is used to select the imaging range of each channel at their respective locations, and generate the complex A-line signals that can be used to create intensity and functional contrasts. To conduct subpixel alignment of the 2 channels, the interferogram $I'_{k\_co}(n)$ from the co-polarization channel is multiplied by a linear phase term $\exp(i\xi \cdot 2\pi n/N)$, where N is the total pixel number of the spectrum and ξ ($|\xi| < 1$) is a constant coefficient used to provide subpixel displacement adjustment δz in the spatial domain, according to the Fourier transform shift theorem. In the discrete Fourier transform, subpixel displacement is manifested as a phase change of the complex A-line signal without significantly altering its magnitude [35]. It thus can be used to align the initial phases of the 2 channels. The calibration coefficient ξ is determined by an iterative process: a mirror is placed in the focal plane of the sample arm to create a single reflector. Its intensity profile will be at the same location in the cross- and co-polarization channels after windowing, and ξ is adjusted until the phase difference at the single reflector location from the 2 channels reaches a minimum value, as illustrated in Figure 2B. It should be noted that this is a one-time calibration step and the coefficient ξ will be fixed if the path length offset between RM1 and RM2 is not altered.

$$\begin{aligned}\overrightarrow{\mathbf{E}_{sn}} &= \frac{\sqrt{R(z_n)}}{2}\mathbf{J}(\delta,\theta)\cdot\mathbf{J}(\delta,\theta)\cdot\mathbf{E} = \frac{\sqrt{R(z_n)}}{2}\begin{bmatrix}\cos\theta\sin\theta[1-\exp(-i2\delta)]\\ \sin^2\theta+\cos^2\theta\exp(-i2\delta)\end{bmatrix}\\ &= \frac{\sqrt{R(z_n)}}{2}\begin{bmatrix}\sin 2\theta\sin\delta\exp\left[i\left(\frac{\pi}{2}-\delta\right)\right]\\ \sqrt{\cos^2\delta+\cos^2 2\theta\sin^2\delta}\exp\left[-i\left(\tan^{-1}\left(\frac{\sin\delta\cos 2\theta}{\cos\delta}\right)+\delta\right)\right]\end{bmatrix},\end{aligned} \quad (4)$$

Furthermore, due to the signal fall-off at the spectrometer, the magnitude of co-polarization A-line signal $I_{co}(z)$ is modified by a constant gain of 6 dB. This gain is determined according to the sensitivity fall-off measurement of the system, which indicates a 6-dB fall-off range of 0.89 mm, and a 12-dB fall-off at around 1.6 mm.

2.3 | Reconstruction of functional contrasts

CP-OCT produces a qualitative contrast describing the depolarization of the incident linearly polarized light, calculated by taking the ratio between the cross- and co-polarization channels as $I_{ratio} = A_x/A_y$. According to Schmitt and Xiang [28], the depolarization effect is characterized by a significant intensity drop in the co-polarization channel, which gives rise to a higher ratio between the cross- and co-polarization intensity signals along the A-line profile. We therefore construct the ratio image to qualitatively present the tissue polarization property. The ratio image is thresholded from 0.3 to 2 for presentation. Due to the imperfect polarization of incident light from supercontinuum source, the lower bound of the threshold for I_{ratio} is determined by the extinction ratio of the 2 channels as indicated in Figure 2B. The upper bound is determined based on empirical observation.

In addition to the ratio image, 2 auxiliary parameters α and β are defined based on Eqs. (2) and (4):

$$\alpha = \frac{\sin\delta\cos 2\theta}{\cos\delta} = \cot(\Phi_y - \Phi_x),$$
$$\beta = \frac{\sqrt{\cos^2\delta + \cos^2 2\theta \sin^2\delta}}{\sin 2\theta \sin\delta} = \frac{A_y}{A_x}. \quad (5)$$

They are used to compute the cumulative phase retardation δ and optic axis orientation θ as

$$\delta(z) = \sin^{-1}\left(\sqrt{\frac{\alpha^2\beta^2 + \alpha^2 + 1}{(\alpha^2+1)\cdot(\beta^2+1)}}\right),$$
$$\theta(z) = \frac{1}{2}\sin^{-1}\left(\sqrt{\frac{\alpha^2+1}{\alpha^2\beta^2+\alpha^2+1}}\right). \quad (6)$$

The ambiguity for δ is 0 to $\pi/2$ and is 0 to $\pi/4$ for θ. It should be noted that the ambiguity of the cumulative optic axis orientation θ is one-fourth of what is offered by the conventional PS-OCT system. Moreover, Eq. (4) also indicates θ will become unmeasurable when δ reaches 0. Hence, we neglect the cumulative optic axis orientation, θ, in our study, and only extract the cumulative retardation. The retardation image I_{ret} is color-coded from 0 to $\pi/2$ to compare with the intensity contrast image $I_{\text{tot}} = \left(A_x^2 + A_y^2\right)^{1/2}$.

2.4 | Sample preparation and imaging protocol

OCT datasets were generated ex vivo from fresh human heart specimens. Human hearts (n = 10) were acquired from the National Disease Research Interchange (NDRI) protocol within 24 hours of donor death. The inclusion criteria for the NDRI protocol are based on the following diagnosis: end stage heart failure, cardiomyopathy, coronary heart disease, amyloid, atrial fibrillation and myocardial infarction. The age, mean ± SD, of the human donors was 62 ± 9, with medical histories including diabetes (30%), cardiomyopathy (60%), hypertension (40%) and heart failure (20%). Three hearts were used to create RFA lesions ex vivo. The RFA treatment follows the procedures described in Ref. [36]. Briefly, all tissues were supra-perfused with temperature-maintained (37° C) phosphate-buffered saline under pulsatile flow. Ablations were performed with temperature regulation by using a commercial RFA system (Stockert 70, Biosense Webster, Diamond Bar, California), and the RFA catheter was placed in contact with the tissue surface. The ablation power was set at 30 W and the target temperature was 65°C to ensure tissue necrosis.

The right ventricle septum is a typical location to acquire EMB samples [6]. For each heart sample, 2 to 3 tissue wedges with 1 cm^3 in size were excised from RVS upon specimen delivery, and OCT imaging was conducted immediately from the endocardium side. The incident power on the sample was 10 mW. All measurements were completed within 48 hours of the donor death.

OCT datasets were acquired at a line rate of 32 kHz using a customized software written in LabVIEW, and later processed in MATLAB (MathWorks, Natick, MA, USA). A single OCT

B-scan contains 800 pixels, covering 3 mm laterally. After processing, there will be 5 output images in total, including cross- and co-polarization OCT images I_{cr} and I_{co}, the reflectivity image or intensity contrast I_{tot}, the cumulative phase retardation image I_{ret} and the ratio image I_{ratio}. The image depth is reduced to 450 pixels due to windowing, covering a depth range of around 0.78 mm in air. All OCT datasets are averaged by 5 times to reduce noise, and the arithmetic means are used to present as B-scans. And all OCT images are presented without scaling for the tissue refractive index.

2.5 | Histology

After imaging, samples were excised into blocks and put into 10% formalin for 24 hour fixation. Histology slides were prepared in the same orientation as a single B-scan. Three to 5 levels were taken from each sample block, and were processed with Masson's Trichrome stain. The slide thickness was 5 μm and spacing between levels was 250 μm. A Leica SCN400 (Leica microsystems, Wetzlar, Germany) slide scanner with ×40 magnification was used to scan and digitize all histology slides. The digitized slides were analyzed by a cardiovascular pathologist blinded to the OCT images using ImageScope (Leica, Wetzlar, Germany). Histology slides were matched with OCT intensity contrast by looking for the similar features within first 300 μm beneath the tissue surface.

2.6 | Statistics

CP-OCT ratio images from the RVS of 6 heart samples that have been confirmed to have corresponding histology slides were included in the statistical study. For every ratio image (800 pixels in lateral direction and 450 pixels in axial direction), every 20 A-lines were grouped and averaged to smooth out the noise. The selected ratio images covered 3 different tissue types in myocardium, including normal myocardium ($n = 14$), mild myocardium fibrosis ($n = 4$) and RFA lesion ($n = 5$). A-line features were extracted from a least-squared fitting process for pixels ranging from the tissue-air interface to the noise floor. The resulted fitting parameters, including the slope, intercept and R-squared value, were used as A-line features. Analysis of variance (ANOVA) with Tukey's multiple comparison test was performed on these features using a commercial software (GraphPad Prism 7.0a, GraphPad Software, Inc, La Jolla, CA, USA), and P–value less than .05 was considered statistically significant.

3 | RESULTS

3.1 | System characterization and validation of polarization measurement

The axial resolution of the system, which is defined as the Full-width half-maximum (FWHM) of the axial Point-spread function (PSF), is measured to be 2.72 μm and drops to 3.07 μm at 0.8 mm. Since 2 polarization channels are multiplexed in depth and the total reflection image I_{tot} is generated based on both channels, the resulting axial resolution of I_{tot} is 3.07 μm.

To validate the accuracy of the polarization measurement performed by the CP-OCT system, we inserted an achromatic quarter wave plate (Thorlabs AQWP05M-980, Thorlabs, Newton, NJ, USA) into the collimated beam of the sample arm and following the steps mentioned

elsewhere [33]. As shown in Figure 3, by rotating the quarter wave plate from 0° to 90°, the measured retardation is 86.6° ± 2.2° for different quarter wave plate settings. The measured optic axis orientation also appears approximately linear against the preset values, while showing an ambiguity of 45°. The results agree with the expectations with minor deviation, which indicates the reconstruction of the polarization properties is working properly. The inaccuracy mainly stems from the channel cross-talk, which is due to the partially polarized light of supercontinuum output after passing through the thin-film linear polarizer.

3.2 | Ex vivo functional CP-OCT imaging of fresh human myocardium

Different tissue types found in the endomyocardial side of RVS are presented in Figures 4 and 5. For each case, 4 images, including the total intensity image, cumulative phase retardation image, ratio image and corresponding histology are presented. The functional OCT images were all thresholded by an intensity mask to remove the background (gray color). As a qualitative contrast, the ratio image is overlaid with the corresponding intensity image. During the experiment, the intensity contrast of the CP channel was optimized by rotating the tissue specimens before taking the images.

At 800 nm window, the photon penetration depth is small within the myocardium. In some cases where the endocardium layer is too thick, only the features in the endocardium layer can be resolved in OCT. Figure 4 shows different features of endocardium. In Figure 4A–D, the endocardial scar in the endocardium layer, which is pointed out in the histology slide in Figure 4A, is well delineated from the normal myocardium in both the structural and functional OCT images (Figure 4B–D). In the retardation image (Figure 4C) and the ratio image (Figure 4D), the fibrosis region that contains, appears to possess a very strong birefringence in comparison with the neighboring normal myocardium. Figure 4E–H illustrate a thickened endocardium region with underlying fibrotic tissue. Differing from the localized endocardial fibrosis, the thickened endocardium does not manifest strong phase retardation. The difference within the CP-OCT-derived images suggests a different tissue composition of the thickened endocardium from endocardial fibrosis, which are hardly noticeable from the intensity images alone. In this case, because the thickened endocardium layer and the underlying mild subendocardial fibrosis scatter most of the light, the signal penetration becomes limited, and it barely reaches the myocardium. Figure 4I–L present an example of localized dense endocardial fibrosis on top of normal myocardium. The endocardial fibrosis is marked by the blue and fibrillar content in the histology slide. The dense collagen content of the fibrotic tissue induces strong retardation, which makes it more visible in functional images but not in the intensity images. It should be noted that the OCT images are not scaled by the refractive index of the tissue, and have asymmetrical scale bars along the A-line and B-scan direction.

Figure 5 shows different tissue types presented in the myocardium. Thanks to the HR provided by the system, microstructures such as the thin endocardium in Figure 5F and the elastic fibers in Figure 5J in the myocardium are clearly visible. In Figure 5A–D, the myocardium is intentionally treated by RFA procedure to create lesion. The lesion region can be delineated by the deep purple region in the histology in Figure 5A. From the intensity image in Figure 5B, we can identify the lesion region by the microtears presented in the

myocardium. Moreover, from the retardation image in Figure 5C, we can see that the lesion region barely manifests birefringence. Similarly, the ratio image shows a very low Cr/Co value in the lesion area, which could be hardly separated from the intensity image background in Figure 5D. It indicates that the polarization state of backscattered light almost maintains the same as that of the incident light, suggesting isotropic tissue architecture of the lesion area. Figure 5E–H demonstrate an example of mild diffuse interstitial myocardial fibrosis. It is marked by a diffuse distribution of fibroblasts within normal cardiomyocytes in the histology. In contrast to the constantly low ratio in the acutely created RFA lesion, the increased signal in the ratio image (Figure 5H) implies that the polarization state of the backscattered light is altered by the fibrotic myocardium. The tissue composition of the fibrotic myocardium could be clearly distinguished from that of the normal myocardium as shown in Figure 5I–L. The normal myocardium manifests birefringence, which results in a gradual increase in the cumulated retardation along the depth (Figure 5K), as well as an increased contrast toward the deeper region of the myocardium in the ratio image (Figure 5L). This observation is consistent with what is depicted by right side of the B-scans in Figure 4C,D,K–L.

3.3 | A-line-based analysis of necrosis, fibrosis and normal myocardium

We have presented that different tissue types found in endocardium and myocardium manifest distinctive functional contrasts within CP-OCT images. Particularly, the ratio image could provide similar contrast as the cumulative retardation image, while it is much easier to obtain. We further explore the contrasts for different myocardial tissue types from the perspective of A-line signals. A-line features of those tissue types are depicted in Figure 6. Figure 6A shows a transition area from an RFA-created lesion to the normal myocardium. Representative A-lines are taken from the green and yellow regions in Figure 6A to illustrate the difference in the signal strengths of cross- and co-polarization channels between the lesion area and the normal myocardium as in Figure 6C,D, respectively. In these 2 cases, the signal strength of the co-polarization channel is in general higher than that of the CP channel. RFA-treated myocardium contains necrotic tissue, which is more isotropic. As a result, the signal ratio between the 2 polarization channels approximately stays constant along the depth, as seen in Figure 6C. On the contrary, in the normal myocardium, due to tissue birefringence, the gradual increase of ratio between the cross- and co-polarization intensities along the depth in Figure 6D. This is also in accordance with the retardation contrast. More interestingly, A-line signals in Figure 6E taken from the blue region in Figure 6B present some unique patterns that are associated with fibrotic myocardium: A-line signals from the 2 channels are almost comparable; and there is a drop (~10 dB) on the co-polarization channel signal strength, which is not presented in previous 2 cases. Moreover, the ratio contrast barely changes during the rotational alignment between the sample and the incident polarization state. According to Schmitt's report on the behavior of cross-polarizers [28], which also resulted in a profound decrease in the signal strength of the co-polarization channel as well as a raise in the ratio, this phenomenon may suggest that the fibrosis region of the myocardium contains CP scatters that depolarize the incident light.

Quantitatively, we extract A-line features, including the slope, intercept and R-squared value, from a least-squared fitting process. The fitting includes pixels from the tissue-air

interface to the noise floor. A-lines with over exposure are excluded from the analysis. In this preliminary study, 3 different A-line features from normal myocardium (n = 517), fibrotic myocardium (n = 152) and RFA lesion (n = 183) are used to perform ANOVA test. The fibrotic myocardium can be well distinguished against normal myocardium based on the all 3 features with $P < .0001$. For example, the intercept is significantly higher ($P < .0001$) for normal myocardium (0.43 ± 0.23) than that for areas of fibrotic myocardium (0.12 ± 0.11) and ablation lesions (0.18 ± 0.08). The intercept also shows difference ($P < .05$) for lesion areas compared with that for fibrotic myocardium. And the R-squared value is much lower ($P < .0001$) for fitted A-lines in normal myocardium (0.61 ± 0.24) than those in fibrotic myocardium (0.73 ± 0.08) and ablated lesions (0.77 ± 0.08).

4 | DISCUSSION AND CONCLUSION

In summary, we presented a single-channel HR CP-OCT system. This system can provide intensity and functional contrasts of human myocardium in one-shot measurement. The co- and cross-polarization channels can be extracted from one single OCT measurement by windowing. The system is characterized to have an axial resolution of 3.07 μm. In addition to the intensity contrast, 2 functional contrasts are reconstructed from the complex A-line signals that are recorded from the cross- and co-polarization channels, including the cumulative retardation and intensity ratio. The cumulative retardation is obtained by using a method adopted in PS-OCT, and the accuracy of the polarization measurement is calibrated by measuring a quarter wave plate at different fast-axis orientations. The intensity ratio between cross- and co-polarization channel intensities is correlated with the depolarization effect. If we compare the cumulative phase retardation image with the ratio image case-by-case, the 2 images offer similar contrast. It suggests a possibility to solely use the ratio image as functional contrast. This could substantially reduce the computational cost caused by the reconstruction of retardation and fulfill the needs for real-time process of large volumetric data. Different tissue types from the endomyocardial side of the RVS are analyzed using the contrasts provided by CP-OCT. We show that the functional contrasts successfully depict the differences in structures and tissue compositions, including localized dense endocardial fibrosis and scar, thickened endocardium, ablated lesion, fibrotic myocardium and normal myocardium. Compared with the intensity image alone, functional contrast may provide additional information regarding the tissue composition in terms of tissue polarization properties. Specifically, fibrotic myocardium is differentiated against the normal myocardium and acute ablated lesion, based on the CP-OCT contrasts.

Previous investigations have reported that normal cardiomyocytes would be destroyed following successful RFA treatment, making the myocardial substrate more homogenous and leading to the absence of phase retardation [7, 20, 24, 36]. In our CP-OCT study, we have observed the same phenomenon from the ablation lesions created within fresh human myocardium samples. More interestingly, the intensity ratio analysis from CP-OCT indicates that diffuse interstitial myocardial fibrosis may manifest depolarization effect based on previously reported phantom study by Schmitt and Xiang [28]. Although further investigation is needed, this observation suggests that the increased fibroblasts in the myocardium may serve as cross-polarizers that eventually lead to the depolarization of light. Moreover, we also demonstrate that the differences between the A-line signals from 2

orthogonal polarization channels can be used to distinguish normal myocardium from the ablated lesion and fibrosis regions. It could be further fed to the tissue classifiers as a new input feature [23], and could offer a rapid and cost-efficient solution to tissue classification for the myocardium.

Nevertheless, there are also some limitations of the proposed CP-OCT system. First, the CP-OCT contrast for birefringent tissue is based on the assumption of uniform optic axis orientation along the depth. This assumption may not hold in the case of complicated tissue composition such as myocardial fibrosis, where multiple types of birefringent tissues are mixed and randomly aligned. As a result, the cumulative retardation reconstructed from CP-OCT may lose its quantitative meaning. Moreover, because of the coupling of retardation and optic axis orientation in the CP channel, the reconstructed optic axis orientation has a degree of ambiguity and hence discarded in our study. This information, however, can be very useful in extracting myofiber orientation as offered by HR PS-OCT-based optical tractography [14, 37, 38]. In addition, it might be very complicated to extract local birefringence based on the CP-OCT measurements, which otherwise can be readily obtained in PS-OCT [39]. Second, due to the coupling between the retardation and optic axis orientation as shown in Eq. (4), rotating the sample or the incident polarization state is necessary to optimize the ratio contrast for birefringent tissue. In addition, the depth range of the resulted CP-OCT images is reduced to 0.78 mm due to channel multiplexing. It may limit the feasibility of this system in other biological tissue imaging applications where a large image range is desired. Techniques like full-range OCT [40] can be applied to extend the image range to overcome this limitation. In this preliminary study, only 2 heart samples manifested myocardial fibrosis. The limited size of dataset hinders a more comprehensive statistical analysis and classification of tissue types based on different Aline features, however, suggests potential for CP-OCT-derived A-line features. In the future, with increased sample size, we will develop classification algorithms to improve detection of fibrotic myocardium with added information provided by multicontrast CP-OCT. In addition, we will explore the role of CP-OCT to provide contrast to identify amyloids, which is an important feature to detect within endomyocardial biopsies [4].

In conclusion, we develop a HR CP-OCT system at 800 nm to differentiate different tissue types in the myocardium by using the polarization-related functional contrasts. This system features a single detection channel and one-shot measurement, and offers qualitative contrasts for differentiation of different human myocardial substrate. The HR CPOCT system provides a new form of polarization-related contrast to differentiate myocardial fibrosis, which is an important substrate to identify during diagnostic and therapeutic procedures.

ACKNOWLEDGMENTS

The authors thank Rajinder Singh-Moon for helping with the radio-frequency ablation procedure and human heart dissection. The work is funded by National Institute of Health (NIH) 1DP2HL127776–01 (C.P.H.), and National Science Foundation (NSF) CAREER Award 1454365 (C.P.H.).

Funding information

National Science Foundation (NSF); National Institutes of Health (NIH), Grant/Award number: 1DP2HL127776–01

REFERENCES

[1]. Nathan M, Ying LC, Pierre C, David B, João L, J. Am. Coll. Cardiol 2011, 57, 891. [PubMed: 21329834]

[2]. Ciulla M, Paliotti R, Hess DB, Tjahja E, Campbell SE, Magrini F, Weber KT, J. Am. Soc. Echocardiogr 1997, 10(6), 657. [PubMed: 9282355]

[3]. Nahrendorf M, Badea C, Hedlund LW, Figueiredo J-L, Sosnovik DE, Johnson GA, Weissleder R, Am. J. Phys. Heart Circ. Phys 2007, 292, H3172.

[4]. Cooper LT, Baughman KL, Feldman AM, Frustaci A, Jessup M, Kuhl U, Levine GN, Narula J, Starling RC, Towbin J, Virmani R, Circulation 2007, 116, 2216. [PubMed: 17959655]

[5]. Saraiva F, Matos V, Gonçalves L, Antunes M, Proviência L, Transplant. Proc 2011, 43, 1908. [PubMed: 21693299]

[6]. From AM, Maleszewski JJ, Rihal CS, Mayo Clin. Proc 2011, 86, 1095. [PubMed: 22033254]

[7]. Fleming CP, Quan KJ, Wang H, Amit G, Rollins AM, Opt. Express 2010, 18, 3079. [PubMed: 20174138]

[8]. Gan Y, Fleming CP, Biomed. Opt. Express 2013, 4, 2150. [PubMed: 24156071]

[9]. Cua M, Lin E, Lee L, Sheng X, Wong KSK, Tibbits GF, Beg MF, Sarunic MV, J. Biomed. Opt 2014, 19, 116007. [PubMed: 25393967]

[10]. Yao X, Gan Y, Marboe CC, Hendon CP, J. Biomed. Opt 2016, 21, 061006.

[11]. Goergen CJ, Chen HH, Sakadžić S, Srinivasan VJ, Sosnovik DE, Phys. Rep 2016, 4, e12894.

[12]. Goergen CJ, Radhakrishnan H, Sakadžić S, Mandeville ET, Lo EH, Sosnovik DE, Srinivasan VJ, Opt. Lett 2012, 37, 3882. [PubMed: 23041891]

[13]. Fan C, Yao G, Biomed. Opt. Express 2013, 4, 460. [PubMed: 23504508]

[14]. Wang Y, Yao G, Biomed. Opt. Express 2013, 4, 2540. [PubMed: 24298414]

[15]. Wang S, Lopez A, Morikawa Y, Tao G, Li J, Larina I, Martin J,Larin K, Biomed. Opt. Express 2014, 5, 1980. [PubMed: 25071943]

[16]. Sun CW, Wang YM, Lu LS, Lu CW, Hsu IJ, Tsai MT, Yang CC, Kiang YW, Wu CC, J. Biomed. Opt 2006, 11, 054016. [PubMed: 17092165]

[17]. Fleming CP, Rosenthal N, Rollins AM, Arruda M, Innovations J Cardiac Rhythm Manage 2011, 2, 199.

[18]. Peterson LM, Jenkins MW, Gu S, Barwick L, Watanabe M, Rollins AM, Biomed. Opt. Express 2012, 3, 3022. [PubMed: 23162737]

[19]. Wang S, Lakomy DS, Garcia MD, Lopez AL, Larin KV, Larina IV, J. Biophotonics 2016, 9, 837. [PubMed: 26996292]

[20]. Fu X, Wang Z, Wang H, Wang YT, Jenkins MW, Rollins AM, Opt. Lett 2014, 39, 5066. [PubMed: 25166075]

[21]. Mekkaoui C, Huang S, Chen HH, Dai G, Reese TG, Kostis WJ, Thiagalingam A, Maurovich-Horvat P, Ruskin JN, Hoffmann U, Jackowski MP, Sosnovik DE, J. Cardiovasc. Magn. Reson 2012, 14(1), 70. [PubMed: 23061749]

[22]. Sosnovik DE, Wang R, Dai G, Wang T, Aikawa E, Novikov M, Rosenzweig A, Gilbert RJ, Wedeen VJ, Circ. Cardiovasc. Imaging 2017, 10(9), 206.

[23]. Gan Y, Yao X, Tsay D, Marboe CC, Hendon CP, Proc. SPIE 2017, 10042, 1004207.

[24]. Ahmad I, Gribble A, Ikram M, Pop M, Vitkin A, Biophotonics J 2016, 9, 750.

[25]. Ghosh N, Wood MFG, Li S-H, Weisel RD, Wilson BC, Li R-K, Vitkin IA, J. Biophotonics 2009, 2, 145. [PubMed: 19343695]

[26]. Tsai M-R, Chiu Y-W, Lo MT, Sun C-K, J. Biomed. Opt 2010, 15, 026002. [PubMed: 20459247]

[27]. Martin TP, Norris G, McConnell G, Currie S, Int. J. Cardiovasc. Imaging 2013, 29, 1733. [PubMed: 23921804]

[28]. Schmitt JM, Xiang SH, Opt. Lett 1998, 23, 1060. [PubMed: 18087429]

[29]. Feldchtein FI, Gelikonov GV, Gelikonov VM, Iksanov RR, Kuranov RV, Sergeev AM, Gladkova ND, Ourutina MN, Warren JA, Reitze DH, Opt. Express 1998, 3, 239. [PubMed: 19384366]

[30]. Gladkova N, Streltsova O, Zagaynova E, Kiseleva E, Gelikonov V, Gelikonov G, Karabut M, Yunusova K, Evdokimova O, J. Biophotonics 2011, 4, 519. [PubMed: 21780300]

[31]. Gubarkova E, Kirillin M, Dudenkova V, Timashev P, Kotova S, Kiseleva E, Timofeeva L, Belkova G, Solovieva A, Moiseev A, Gelikonov G, Fiks I, Feldchtein F, Gladkova N, J. Biomed. Opt 2016, 21, 126010. [PubMed: 27997633]

[32]. Rasmussen K, Reilly C, Li Y, Jones RS, Biotechnol. Bioeng 2016, 113, 198. [PubMed: 26156808]

[33]. Fan C, Wang Y, Wang RK, Opt. Express 2007, 15, 7950. [PubMed: 19547122]

[34]. Hitzenberger CK, Götzinger E, Sticker M, Pircher M, Fercher AF, Biomed. Opt. Express 2001, 9, 780.

[35]. Ling Y, Gan Y, Yao X, Hendon CP, Opt. Lett 2017, 42, 1333. [PubMed: 28362762]

[36]. Singh-Moon RP, Marboe CC, Hendon CP, Biomed. Opt. Express 2015, 6, 2494. [PubMed: 26203376]

[37]. Wang H, Akkin T, Magnain C, Wang R, Dubb J, Kostis WJ, Yaseen MA, Cramer A, Sakadžić S, Boas D, Opt. Lett 2016, 41, 2213. [PubMed: 27176965]

[38]. Fialovć S, Augustin M, Glösmann M, Himmel T, Rauscher S, Gröger M, Pircher M, Hitzenberger CK, Baumann B, Biomed. Opt. Express 2016, 7, 1479. [PubMed: 27446670]

[39]. Fan C, Yao G, Opt. Lett 2012, 37, 1415. [PubMed: 22555689]

[40]. Fan C, Yao G, Opt. Express 2012, 20, 22360. [PubMed: 23037384]

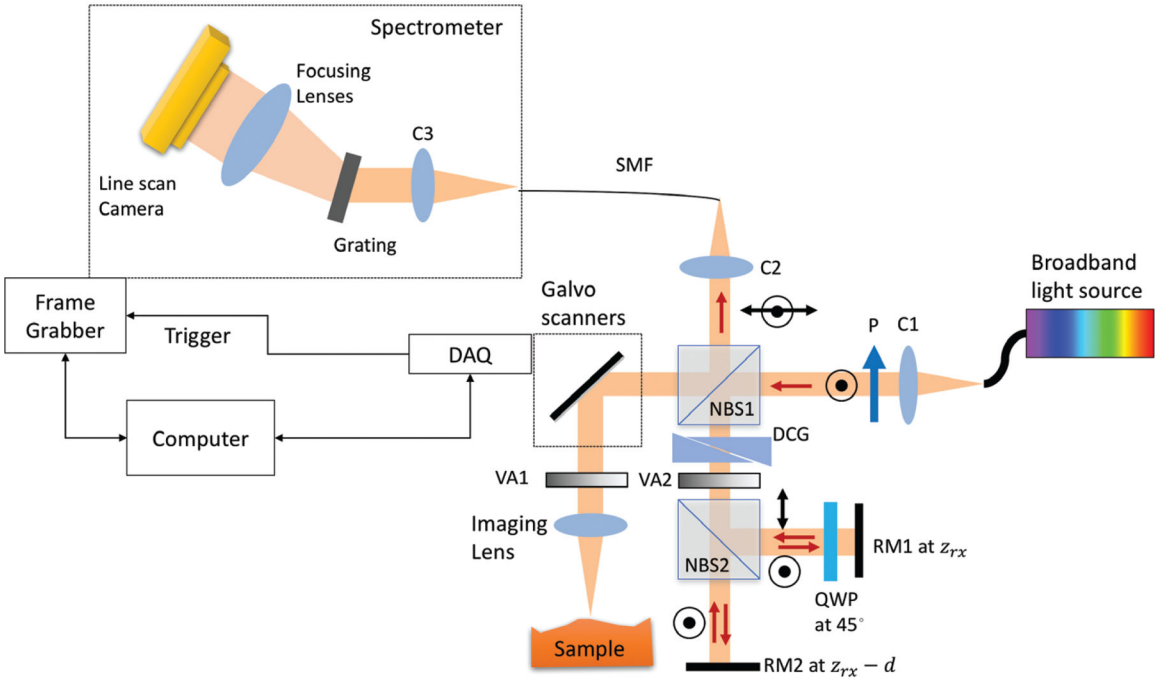

FIGURE 1.

Schematic of HR CP-OCT system. C, Collimation lens; P, polarizer; NBS, nonpolarized beam cube; DCG, dispersion compensation glass; VA, variable attenuator; RM, reference mirror; SMF, single mode fiber; QWP, quarter wave plate; DQ, Data acquisition. The fast axis of QWP was aligned at 45° with respect to the input polarization. Tissue samples are mounted on a 3-axis translation stage with rotating platform

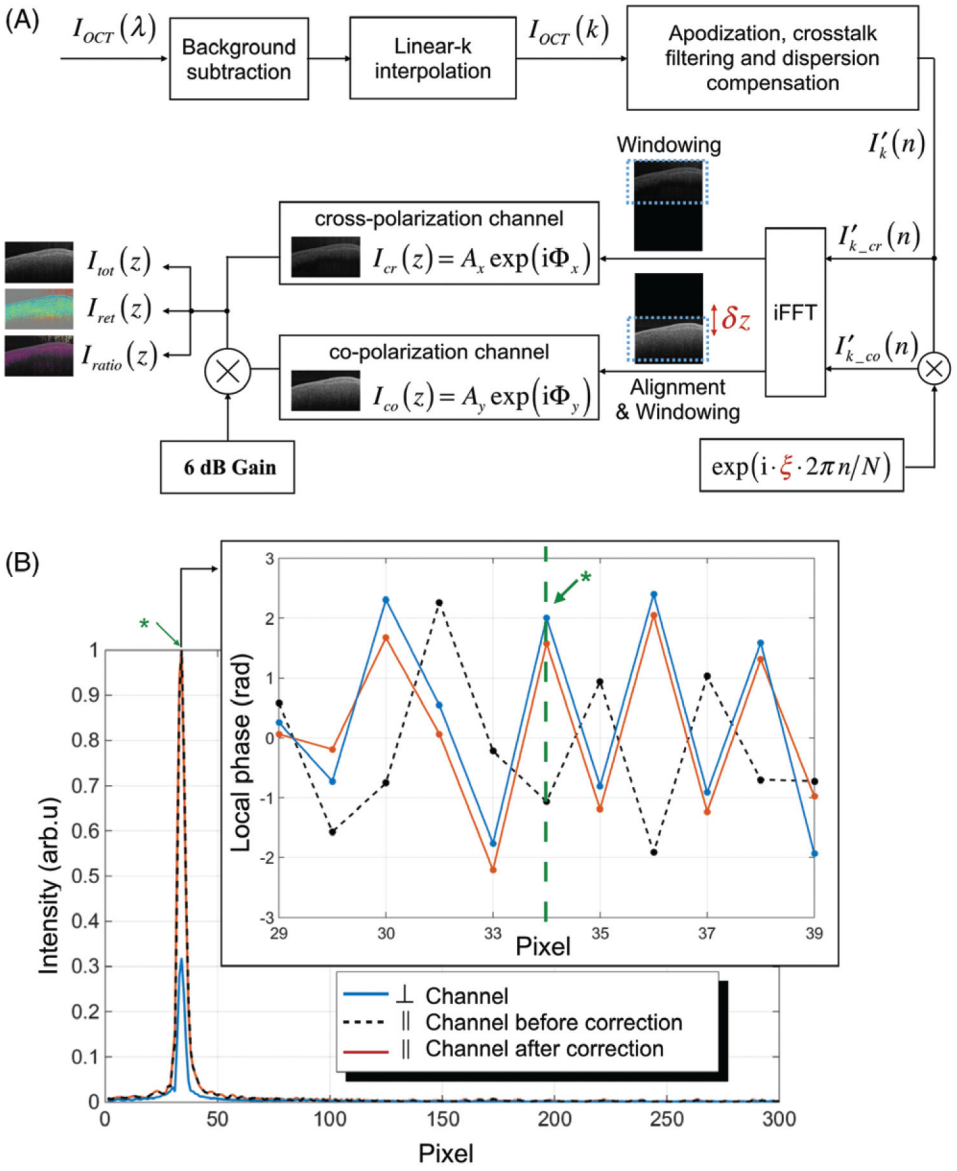

FIGURE 2.

(A), The signal processing flow chart. A calibration coefficient ξ is introduced to the co-polarization channel spectra to perform subpixel alignment of the 2 orthogonal channels, and a 6-dB gain is applied to the co-polarization intensity to compensate for spectrometer sensitivity fall-off. (B), A-line signals with a single reflector in the sample arm before and after fine-alignment. The extinction ratio is about 0.3 resulting from the channel cross-talk, and the alignment does not impact the A-line intensity profile. Inset: Phase adjustment of co-polarization channel. The initial phase mismatch at the location of single reflector (marked by green star) is corrected after alignment

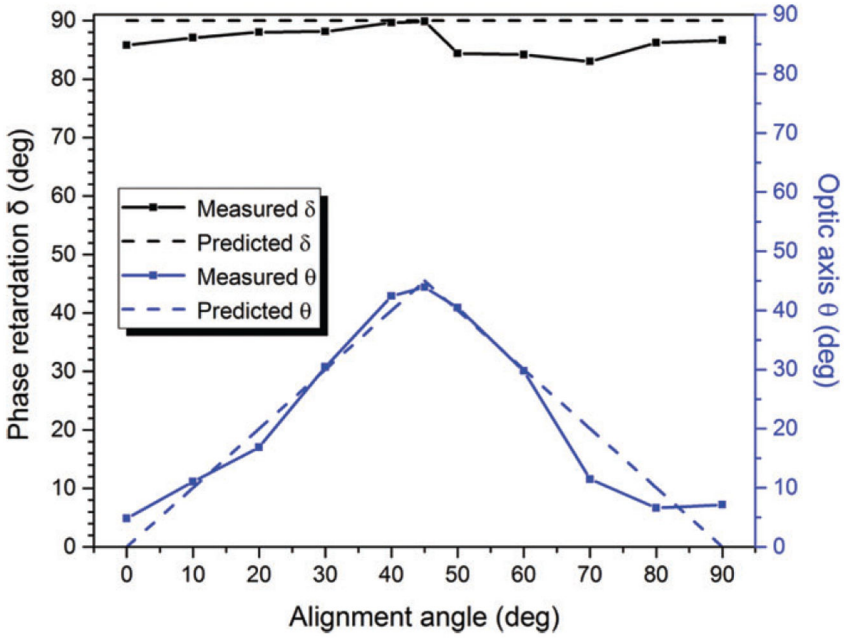

FIGURE 3.

Validation of birefringence measurement by using a quarter wave plate manually aligned at different angles. The measured retardation is 86.6° ± 2.2°, and the optic axis orientation follows linearly with the preset values, with an ambiguity of 45°

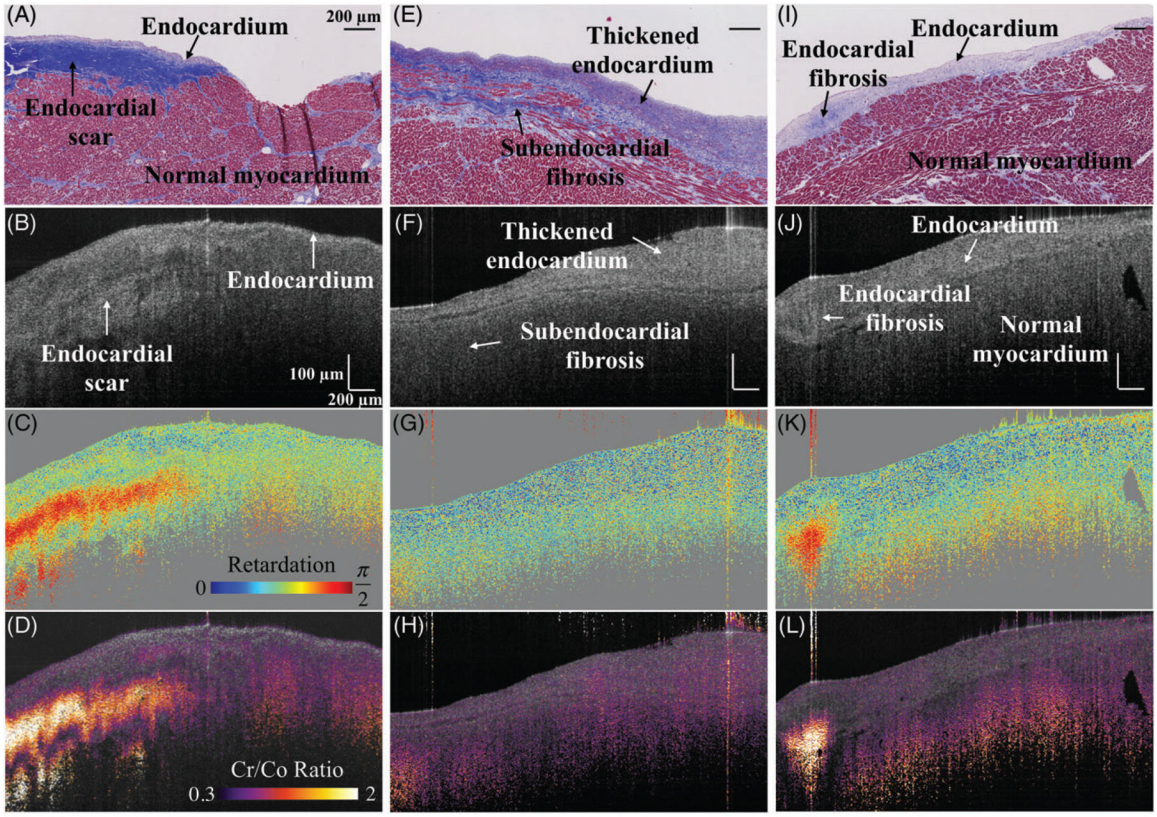

FIGURE 4.

Different features of the endocardium of right ventricular septum from fresh human heart specimens. (A), (E), (I) are the histology slides corresponded to the OCT intensity images. (B), (F), (J) are OCT intensity images that provide structural information. (C), (G), (K) are the cumulative phase retardation images, color-coded from 0 to π/2 with low-SNR regions marked as gray area. The endocardial scar in (C) shows strong cumulative phase retardation due to the presence of densely packed collagen fibers, while the thickened endocardium in (G) barely presents the same feature. Another example of endocardial fibrosis is shown in (K). The dense endocardial fibrosis induces strong retardation because of its collagen content. (D), (H), (L) are the ratio images offering the qualitative contrast, which match well with the retardation contrast. The ratio images are thresholded and color-coded from 0.3 to 2. (A), (E), (I) scale bar: 200 μm. (B), (F), (J) scale bar: (vertical) 100 μm, (horizontal) 200 μm

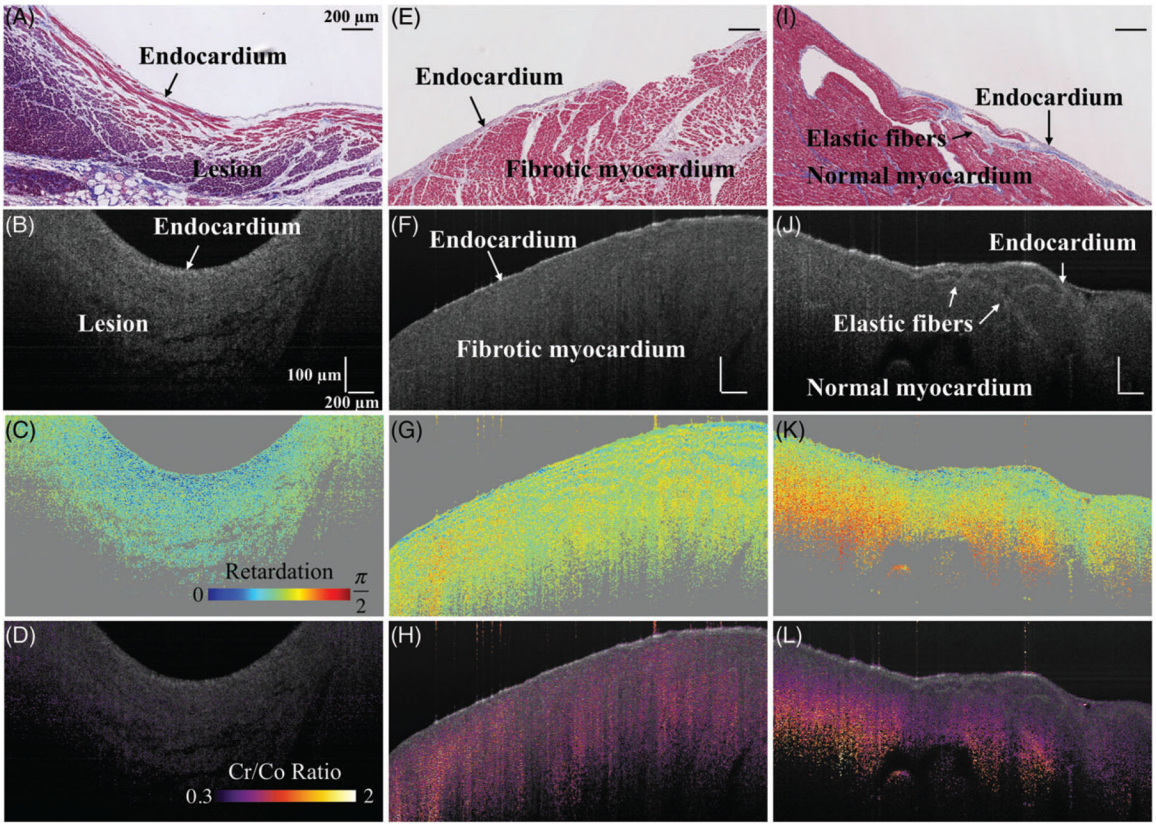

FIGURE 5.

Different tissue types in the myocardium of right ventricular septum from fresh human heart specimens. (A), (E), (I) are the histology slides corresponded to the OCT B-scans. (B), (F), (J) are OCT intensity images that provide structural information. (C), (G), (K) are the retardation images showing the quantitative polarization property of the tissue, color-coded from 0 to π/2 with low-SNR regions marked as gray area. The ablated tissue shows very low cumulative phase retardation in (C), while the normal myocardium manifests increased retardation along the depth shown in (K). The fibrotic tissue, shows an increased Cr/Co ratio over the depth without an apparent gradient in (H), which is quite distinctive compared with the other 2 cases. (D), (H), (L) are the ratio images offering the qualitative contrast, showing good correspondence with the retardation images. Scale bar dimensions are the same as in Figure 4 on p. 26

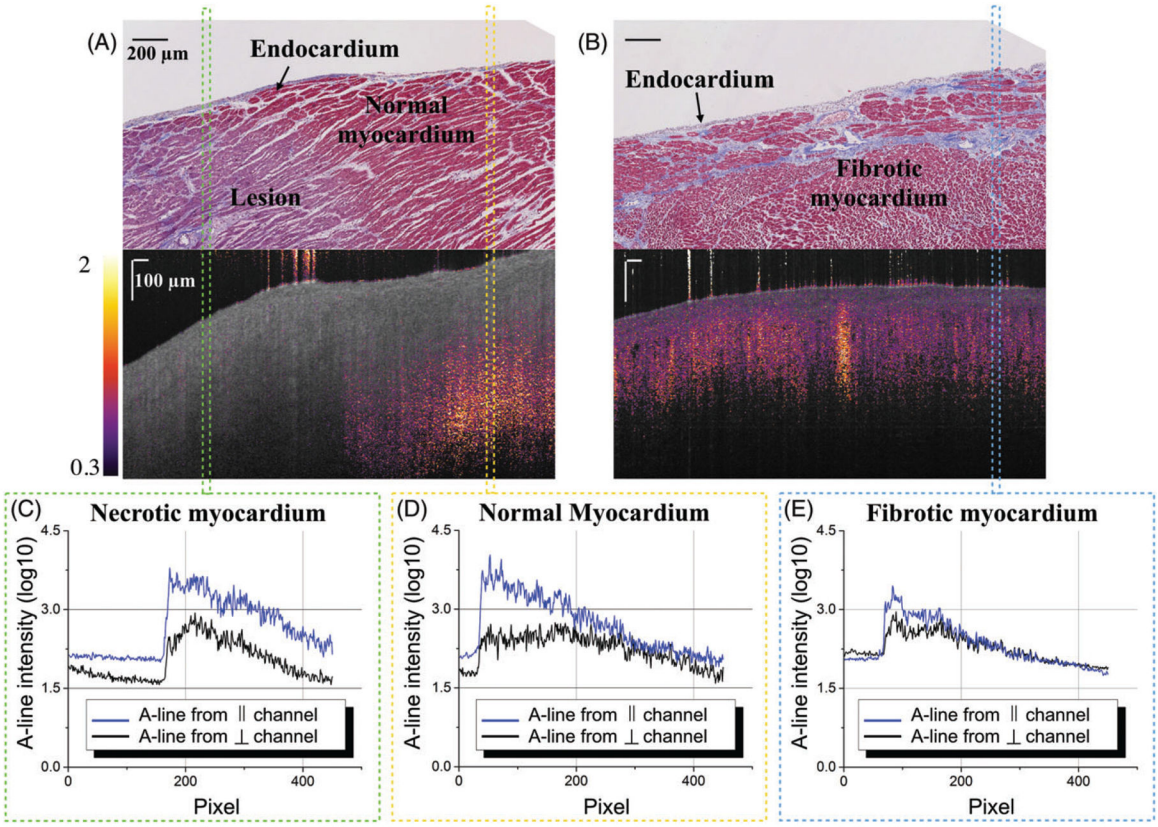

FIGURE 6.

Different A-line signatures of both CP-OCT channels in the ablated lesion, normal myocardium, and fibrotic myocardium regions. Histology slides and the corresponding ratio images are presented for (A) transition region from an RFA-created lesion to normal myocardium, and (B) fibrotic myocardium. Representative A-lines in logarithmic scale from both the cross- and co-polarization channels are selected from (C) the lesion, (D) normal myocardium and (E) fibrotic myocardium, respectively. Five consecutive A-lines are averaged to produce a smoothed profile